*Bin Wang*
*Yuqi Jiao*
*Dongsheng Qiao*
*Shan Gao*
*Tianfei Li*
*Jinping Ou*

http://dx.doi.org/10.21278/brod74208

ISSN 0007-215X
eISSN 1845-5859

# Modified *p-y* curves for monopile foundation with different length-to-diameter ratio

UDC 621.224.3:621.3.016.3:519.64
Original scientific paper

**Summary**

The soil reaction of the monopile foundation subjected to lateral loading in offshore wind turbines is typically assessed relying on *p-y* curves advocated by API. However, this method is inadequate for gradually increasing monopile diameters and significantly underestimates the lateral soil confinement. In the present works, a 3*D* pile-soil interaction finite element model was first established, considering the soil suction and strain hardening characteristics for the normally consolidated clay in China's sea. Modifications to the *p-y* curves in API were accomplished in the comparative process between the lateral soil resistance-displacement curves retrieved from the finite element model and the representative expression. Furthermore, the prediction accuracy for the corrected *p-y* curves has been proved by forecasting the monopile lateral bearing capacity with varying length-to-diameter ratios, which also demonstrates that the modified *p-y* curves could successfully reflect the lateral soil confinement of the normally consolidated clay and flexible piles. It also provides an approach to assess the deformation response and horizontal ultimate bearing capacity of monopiles with different length-to-diameter ratios.

*Key words:* *monopile; p-y curve; length-to-diameter ratio; normally consolidated clay; finite element method*

## 1. Introduction

Over the past decade, China has made significant accomplishments in offshore wind power [1-3]. As the most extensively used wind turbine foundation, large-diameter monopiles have a more straightforward structural form, saving steel and easy installation [4]. Its service environment also determines that monopiles are predominantly loaded by horizontal forces and overturning moments [5-9]. To improve the stability of the wind turbine superstructure, the design of the infrastructure requires a focus on the deformation response and lateral ultimate bearing capacity, in which simulating the monopile-sediment interaction is an essential aspect.

For the study of the lateral response of monopile, the available methods mainly include model tests, the upper-bound methods of plasticity theory, finite element methods, and the Winkle foundation model. Currently, centrifuge tests have been utilized by numerous researchers to investigate lateral responses of various types of piles - flexible, semi-rigid, and rigid - with different shapes and end conditions in soft clay [10-13]. The ultimate restraint of the clay was investigated through the field tests executed by Byrne et al [14] and Zhu et al [15]. Even though the model test is more accurate, it is time-consuming, costly, and only applicable to specific soil profiles, thus making it unable to be adopted as conventional design guidelines. To confirm the horizontal ultimate bearing capacity of the monopile, the upper-bound approaches of plasticity theory [16] were employed by Murff et al [17] to develop a failure mechanism, which has since been improved by Martain et al [18] and Yu et al [19]. The horizontal vibrations of single piles were also constructed on account of Biot wave propagation equations and the Novak thin-layer method [20, 21]. However, these methods can only obtain the ultimate capacity, but the complete load-deformation responses, which are also of great concern in the wind turbine design, are failed to give. As a recommended method for verifying the *p-y* analysis method by DNV [22], the finite element method is capable of effectively modeling the non-linear pile-soil interaction and has been utilized extensively in the pile-foundation response study [10, 23-29]. But the model requires refined mesh and rigorous boundary conditions, and the computational accuracy significantly depends on the calculation time. Hence, the finite element method is unsuitable for designing batch calculations. The most effective way to modify the pile-soil interaction is the Winkle beam method [30, 31], in which the complex soil constitutive model and modeling process can be avoided, and the *p-y* curves are regarded as the decisive element in this model.

The *p-y* spring model advocated by the latest version of the API [32] is based on the on-site test conducted at Sabine River with heavily over-consolidated clays [33]. Markedly different from the North Sea condition, the geological conditions in China typically consist of high-strength clay overlain by normally consolidated soft clay [34], which will complicate the installation process of the turbine foundation and diminishes the compatibility of the *p-y* curves in the API. Therefore, one of the key issues now is to formulate more applicable *p-y* curve expressions for normally consolidated clay to guide monopile foundation design in the offshore industry. Besides, numerous studies indicated that the suggested *p-y* curves underrate the pile-soil interaction behaviors, for which Jeanjean [10] and Templeton [23] have thoroughly investigated the flexible pile-soft clay interaction at different depths based on centrifuge tests and finite element method, upon which a normalized *p-y* curve expression was proposed following the hyperbolic tangent mathematical model of O'Neill et al [35]. Wang et al [29] further considered the impact of length-to-diameter ratios ($L/D$) on the lateral behavior of monopiles. Zhang et al [36, 37] incorporated the NGI-ADP model [38] into their numerical simulation to probe the pile undrained bearing capacity and deformation of the clay. They also investigated the influence of soil stress-strain and pile-soil interface roughness on the resulting *p-y* curves to improve their precision. Murff et al [17] introduced a framework for the lateral bearing capacity factor that can be assessed for the ultimate state of the monopile bearing capacity. Many scholars have modified this parameter since then [12, 19, 24]. All of the refined *p-y* curves can simulate the monopile horizontal behavior. Still, it is noticeable that these analytical solutions are not validated with various length-to-diameter ratios, and their suitability is ambiguous.

To provide an accurate and efficient *p-y* curve between the normally consolidated clay and monopiles with varying length-to-diameter ratios, a finite element pile-soil interaction model is constructed by means of the large commercial finite element simulation software ABAQUS in the present study. The modification of the *p-y* curves advocated by API is accomplished by comparing the lateral force-displacement behavior captured from the

numerical model with the representative expressions. The effects of the clay's strain-hardening and suction properties on the lateral response of the monopile are also investigated.

## 2. Finite element analysis model

### 2.1 Geometry and model set-up

In the present paper, the finite element analysis is performed in the finite element calculation software ABAQUS [39]. As the model and load symmetry here take of the soil domain, shown in Fig.1. The soil domain is taken as 20*D* (*D* is the diameter of the pile) along the radial direction, and the vertical soil boundary is 2.5*D* from the bottom of the pile following the model of Zhang et al [36] to eliminate the scale and boundary condition effects on the computations. The soil domain is simulated by the solid element C3D8R, and the local mesh encryption method is presented in the range of 2*D* from the symmetry center of the model as well as the location near the pile bottom with the minimum mesh size of 0.15*D* to eliminate the interruption of analysis caused by the mesh distortion of the soil element.

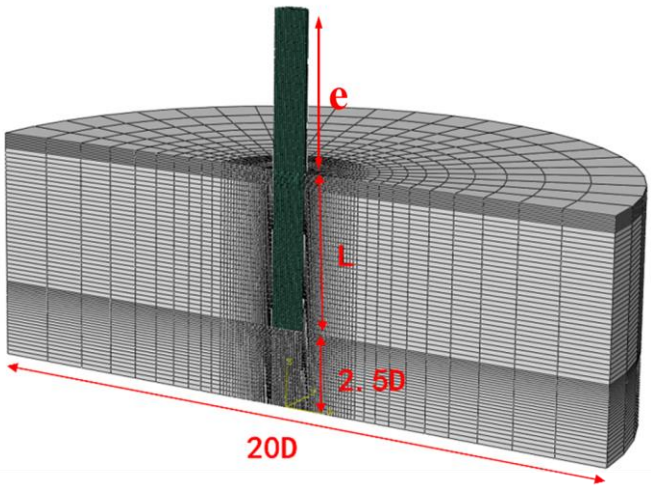


**Fig. 1** Finite elememt model of pile-soil interaction

The monopile refers to the steel pipe pile commonly used in wind turbine foundations with density $\rho_p$=7850g/cm$^3$, elasticity modulus $E_p$=2.06×10$^{11}$Pa, poisson's ratio $v_p$=0.3 and diameter $D$=2.0m, the pile thickness is taken as $t$=0.0267m on the recommendation of the API specification for the thickness of steel pipe pile. The pile free end length is denoted as $e$, and the penetration length of the pile is indicated as $L$. The monopile is discretized by the continuous elements of C3D8R, adopting the suitable mesh size with the contact soil model. To reveal the lateral response of monopiles with different rigidities and embedment depths, thirteen groups of working conditions with $L/D$=2.5~30 are selected in this study according to the criterion of pile rigidity proposed by Poulous et al [40], which consist of three groups of flexible piles (Group I, Table.1), five groups of semi-rigid piles (Group II, Table.1) and five groups of rigid piles(Group III, Table.1), the selected dimensions are assembled in Table.1.

**Table 1** Dimensions performed in the present paper

| Analysis | *L*, m | *L*/*D* | rigidity |
|---|---|---|---|
| Group I | 60, 40 and 30 | 30, 20 and 15 | Flexibility |
| Group II | 24, 20, 16, 14 and 12 | 12, 10, 8, 7 and 6 | Semi-rigid |
| Group III | 10, 8, 7, 6 and 5 | 5,4,3.5,3 and 2.5 | Rigid |

## 2.2 Constitutive law and material properties

In this study, the NGI-ADP elastic-plastic constitutive law is employed to capture the stress versus strain relations of the normally consolidated clay, which adopts the Tresca yield criterion and can reflect the strain-hardening characteristics of the clay by establishing the dependence of the current shear stress $\tau$ on plastic shear strain $\gamma_p$ [38]. The NGI-ADP model's plastic hardening rule can be expressed in the following manner:

$$\frac{\tau}{s_u} = 2\frac{\sqrt{\gamma^p / \gamma_f^p}}{1+\gamma^p / \gamma_f^p} \tag{1}$$

where, $\tau$ is the current shear stress; $s_u$ is the undrained shear strength of the clay; $\gamma^p$is the plastic shear strain; $\gamma^p_f$ is the ultimate plastic shear strain.

The total shear strain $\gamma$ relevant to the current shear stress $\tau$ consists of elastic shear strain $\gamma^e$ and plastic shear strain $\gamma^p$:

$$\gamma = \gamma^e + \gamma^p = \frac{\tau}{G_{\max}} + \gamma^p = \frac{\tau / s_u}{G_{\max} / s_u} + \gamma^p \tag{2}$$

where, $G_{max}$ is the strain shear modulus. $G_{max}/s_u$ is assumed constant throughout.

Fig.2 depicts the stress-strain characteristics of the clay for different peak plastic shear strains. The plastic shear strain $\gamma^p$ causes a rise in shear stress ratios $\tau/s_u$, illustrating that it is appropriate for the NGI-ADP model to reflect the strain hardening of the clay. The ultimate plastic shear strain $\gamma^p_f$ is a vital parameter in the soil response process. It increase with the the improvement of the inflection plastic strain and decrease of the slope of shear stress ratios $\tau/s_u$ in the elastic deformation phase. To detect how the clay strain hardening effects affect the lateral performance of the monopile, the sensitivity analysis about $\gamma^p_f$ will be discussed in the following subsections of this paper.

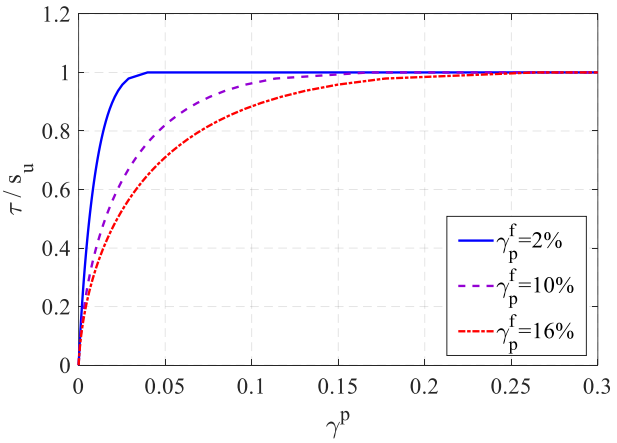


**Fig.2** Stress-strain responses of the clay

For the specific parameters of the normally consolidated clay, the undrained shear stress is taken as $s_u$=104.25kPa with the effective unit weight $\gamma'$=6.0kN/m$^3$, the Poisson's ratio $v_s$=0.49 and the uniform stiffness ratio $E_s/s_u$=1000, the quotient of strain shear modulus and shear strength is further obtained as $G_{max}/s_u$=333 deduced from the equation $G_{max}=E_s$ / 2(1+$v_s$), the ultimate plastic shear strain is adopted as $\gamma^p_f$=2%, 10%,.and 16%. To fully consider the suction of the clay on the pile-soil contact surface, the general contact in ABAQUS has been taken, in which the roughness factor is taken as $\alpha$=1 [37].

## 2.3 Boundary condition and mesh convergence verification

The Mises stress nephograms of the clay are depicted in Fig.3 when the monopile approaches the bearing capacity limited states. It can be seen that there is no stress concentration at the fixed boundary, illustrating the validity of the model size adoption. The soil thrust at the pile's rear is almost the same as the passive pressure at the front because of the consideration of the isotropic damage and the suction condition of the normally consolidated clay.

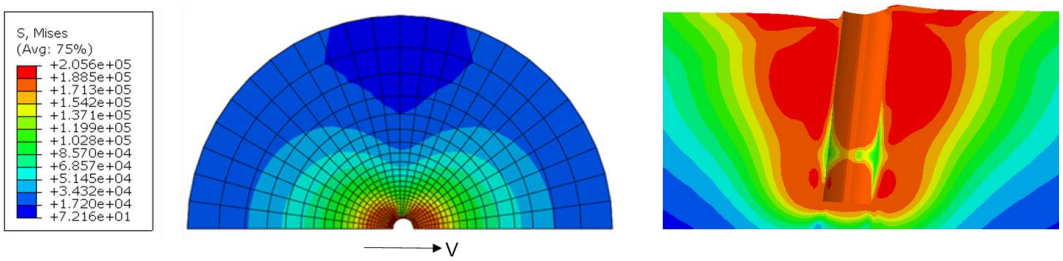


**Fig.3** The Mises stress nephograms of the clay

The mesh convergence has also been conducted to eliminate the impact of mesh size and boundary condition influences on the numerical outcomes. Specifically, put the mesh quantity of the soil domain become sparse or encrypted respectively. Then, compare the horizontal ultimate bearing capacity of the monopile by applying gradually improved displacement at the mud line. Fig.4 shows the monopile mesh convergence verification with $L/D$=5, where the solid red stripe stands for the recommendation of this paper. The mesh size has little impact on the outcomes when the monopile has a small horizontal displacement at the mud line. But as the horizontal displacement continuously increases, the ultimate capacity decreases by 1.5% with further encryption of the mesh to eight times its recommended size, while an eight times increase in the mesh size will produce a more significant error of 6%, thus verifying the mesh convergence.

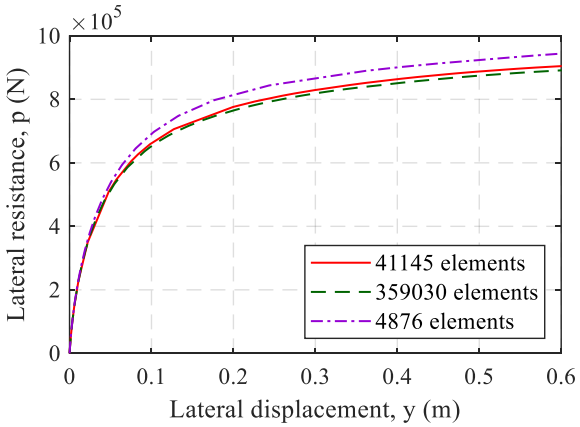


**Fig.4** Mesh convergence verification of the monopile ($L/D$=5)

### 2.4 Simulation of PIAS field test

To illustrate the dependability of the finite element methodology in the present work, the on-site experiments of the PISA project [14] were used for comparative verification, which was carried out in a layered over-consolidated clay with $L/D$=5.52, a pile diameter of $D$=0.762m, a thickness of $t$=11mm, the pile free end length $e$=10m. The soil parameters were converted to NGI-ADP model parameters by the plasticity index method [36], and the roughness factor is taken as $\alpha$=0.3 following the roughness conversion method of API guidelines [32]. Specific soil characteristics are shown in Table 2.

**Table 2** Experimental parameter of the field test by PIAS [14]

| Depth, m | $\gamma'$, kN/m3 | $s_{u,avg}$, kPa | $G$ / $s_{u,avg}$ | $\gamma^{p}_{f}$ |
|---|---|---|---|---|
| 0-2.0 | 11.2 | 40-128 | 500 | 0.2 |
| 2.0-2.7 | 11.2 | 128 | 500 | 0.2 |
| 2.7-4.0 | 11.2 | 104 | 500 | 0.2 |
| 4.0-5.0 | 11.2 | 88 | 500 | 0.2 |
| 5.0-7.6 | 11.2 | 88-104 | 500 | 0.2 |

Following the soil characteristics depicted in Table 2, the numerical simulation model is established and the horizontal forces are exerted at the pile head to measure the horizontal shift at the mud line. The results shown in Fig.5 indicate that the finite element methodology is not only feasible for multi-layered clay but also performs successfully on the lateral load-displacement behaviors of the piles observed in the field test and thus can be promoted as valid values in the subsequent calculations.

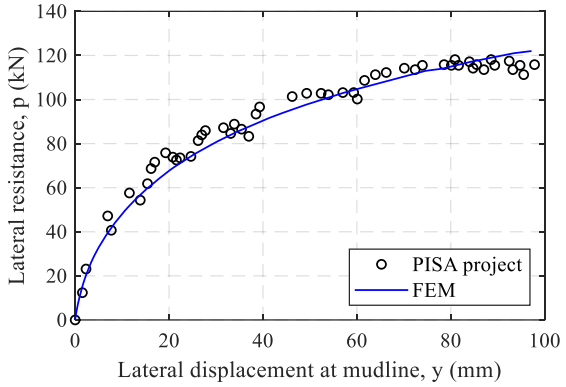


**Fig.5** Verification between finite element model and PISA test

## 3. Numerical result and limitation of the traditional p-y curves

To quantitaticely analyze the lateral response of the monopiles and profoundly understand the limitations of the traditional *p-y* curves, the bearing capacity with different length-to-diameter ratios was firstly calculated. Then, the soil failure mechanism of monopiles in different rigidities are investigated. Finally, the limitations of the traditional *p-y* curves are comprehensively revealed based on the above quantitative and mechanism studies.

### 3.1 Monopile ultimate bearing capacity

It has been shown that the ultimate state of the monopile bearing capacity can be obtained when the displacement at the mud line comes to 0.2$D$ [9, 33]. Therefore, the soil resistance at the mud line, equating to the lateral bearing capacity of the monopile, can be obtained by gradually increasing the displacement at the mud line up to 0.3$D$ under all working conditions. Lateral resistance-displacement responses (*p-y*) of monopiles with

different length-to-diameter ratios are shown in Fig.6, in which the solid lines, dashed lines, and dotted lines correspond to rigid piles, semi-rigid piles and flexible piles, respectively. It is evident from the figure that the bearing capacity of the pile is increased with the increase of horizontal displacement. Slopes on curves, which represent the stiffness of the pile $k$ ($k$=d$p$/d$y$), have decreased with the horizontal displacement increasing until it tends to zero at full plasticity. The smaller the $L/D$, the faster the $k$ decreases due to the different soil damage mechanisms caused by different rigidities. Moreover, the longer the penetration length of pile $L$ is, the larger the ultimate bearing capacity of the pile is in the same diameter. The bearing capacity is almost the same when the penetration length is greater than 15$D$, which is attributed to the fact that when $L<L_{cr}$ ($L_{cr}$ is the critical length of the pile), the bearing capacity is affected by the lateral soil confinement, and when $L>L_{cr}$, the pile beyond this length is affected very slightly and can be regarded as the fixed end approximately.

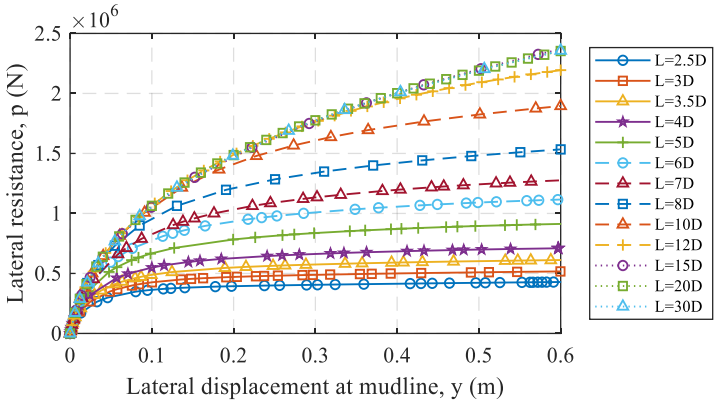


**Fig.6** *P-y* curves extracted from the finite element analysis

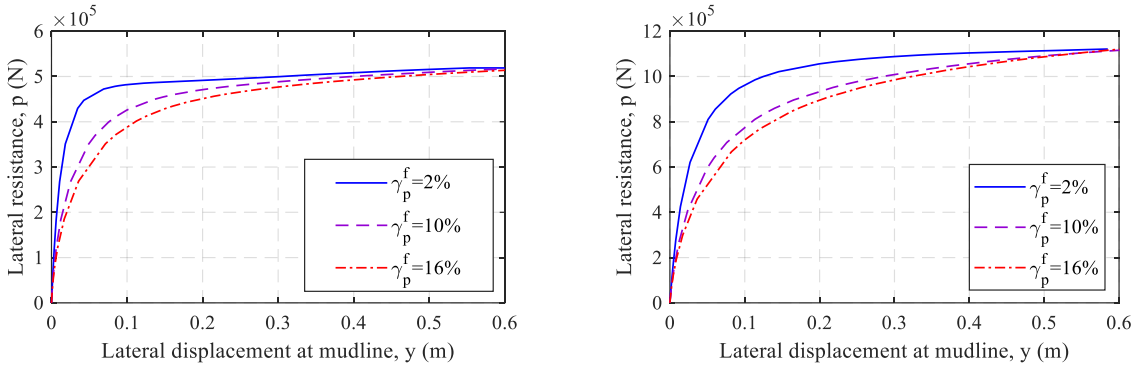


(a) $L/D$=3 (b) $L/D$=6

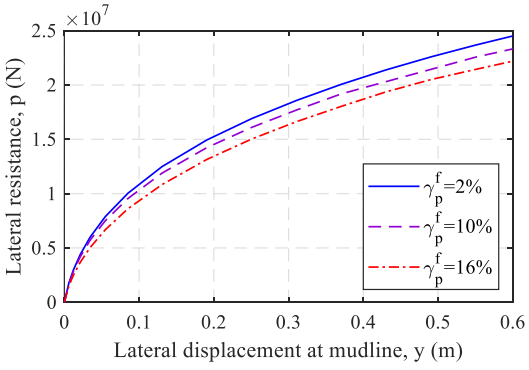


(c) $L/D$=15

**Fig.7** Effect of $\gamma_f{}^p$ on the lateral-displacement response

This paper also calculates the monopile ultimate bearing capacity for $L/D$=3, 6, and 15, and the ultimate plastic shear strain of soil $\gamma^p_f$ =2%, 10%, 16%, as shown in Fig.7. It indicates that the length-to-diameter ratio ($L/D$) reflects the pile rigidity, the higher the pile rigidity, the greater the ultimate bearing capacity, and the scale of the ultimate plastic shear strain also affects the variation rate of the monopile bearing capacity, the lateral load-displacement curves changes more slowly as the ultimate plastic shear strain increase. Its trend has obvious self-similarity with the soil stress-strain relationship shown in Fig.2. Therefore, the soil stress-strain parameters allow to be integrated into the calculation formula of the modified *p-y* analysis methods to reflect the implication of the clay strain hardening for the monopile lateral responses. Soil failure mechanism

Displacement vector nephograms from the ABAQUS post-processing visualization interface are taken to study the soil failure mechanism. Fig.8 (a)-(c) displays the soil failure mechanisms and the pile displacement profiles below the mud line after being subjected to a horizontal displacement of 0.3$D$ with three different rigidity for $L/D$=20, 10, 3.

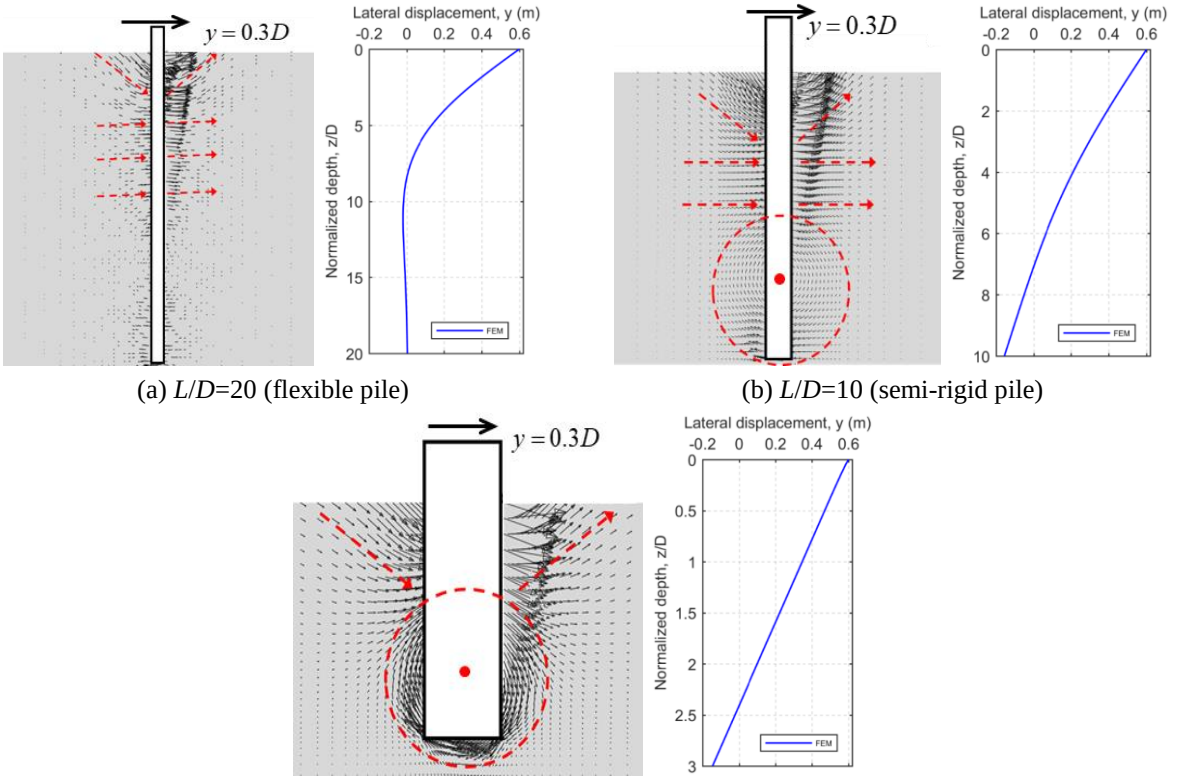


(a) $L/D$=20 (flexible pile) (b) $L/D$=10 (semi-rigid pile)

(c) $L/D$=3 (rigid pile)

**Fig.8** Soil flow mechanisms and displacements of the pile below the mudline

When a significant horizontal displacement is imposed on the flexible pile, as illustrated in Fig. 8(a), the weak soil confinement and the transitional movement from lateral to vertical due to soil compression cause a wedge-type failure surface in the overlying soil area. With further increase in depth, wedge-type flows gradually vanish until the bearing capacity approaches the upper limit, and the full flow mechanism occurs below the wedge. It is the excessive flexural deflection and gradually increasing soil resistance that makes an opposite displacement in the lower part of the pile and two zero displacement regions. When the depth exceeds $L_{cr}$, the pile is confined by the surrounding soil, which is approximately equivalent to the fixed end.

For the semi-rigid pile ($L/D$=10) presented in Fig.8(b), the deflection in the horizontal direction is still predominant near the mud line, and the soil failure mechanisms experience a

flow pattern resembling a wedge close to the soil surface, while a complete flow pattern occurs under the wedge. However, owing to the increased rigidity of the pile, the horizontal displacement demonstrated a nearly linear correlation with depth in the lower section of the pile, with the pile mainly pivoting around the rotation point at $z$=7.1$D$, producing maximum reverse displacement at the base of the pile.

For the monopile ($L$/$D$=3) with greater rigidity shown in Fig.8(c), a rigid rotation around the rotation point at $z$=2.3$D$ occurs after being exposed to a horizontal displacement. The displacement of the rigid pile varies linearly from top to bottom along the depth without any bending deformation, and the largest reverse displacement appears at the bottom of the pile as well. The wedge-type flow of the soil still occurs near the soil surface, which is determined by the compression effect on the surrounding soil rather than the flow mechanism. And because of the short length of the pile, the wedge-type mechanism cannot extend to further depth and no full flow occurs. Instead, a wide range of soil rotation appears to resist the pile rotation, and as the displacement increases, the soil experiences rotational damage.

## 3.2 Limitation of traditional p-y curves

Following the API guidelines, the lateral load-displacement response of monopiles are usually identified by the traditional *p-y* curves, as shown in Fig.9, where $p_u$ is the ultimate lateral bearing capacity of piles; $y_c$ is the corresponding displacement at which the soil has attained half of its ultimate resistance; $\varepsilon_c$ is the strain occurring at half of the maximum deviator stress in undrained compression tests; $J$ is the dimensionless coefficient that falls between 0.25~0.5; $N_p$ is the ultimate bearing capacity factor that is equal to $p_u/(s_uD)$ in numerical terms. The traditional *p-y* method contains two parts: the first part is the normalized p-y curve that controls the profile in the elastic stage ($y/y_c$=0~1, in Fig.9(a)), the elastoplastic stage ($y/y_c$=1~8, in Fig.9(a)) and the plastic stage ($y/y_c$>8, in Fig.9(a)), respectively. The second part is the ultimate lateral bearing capacity $p_u$ controlled by the dimensionless factor $N_p$, determining the magnitude of *p-y* curves.

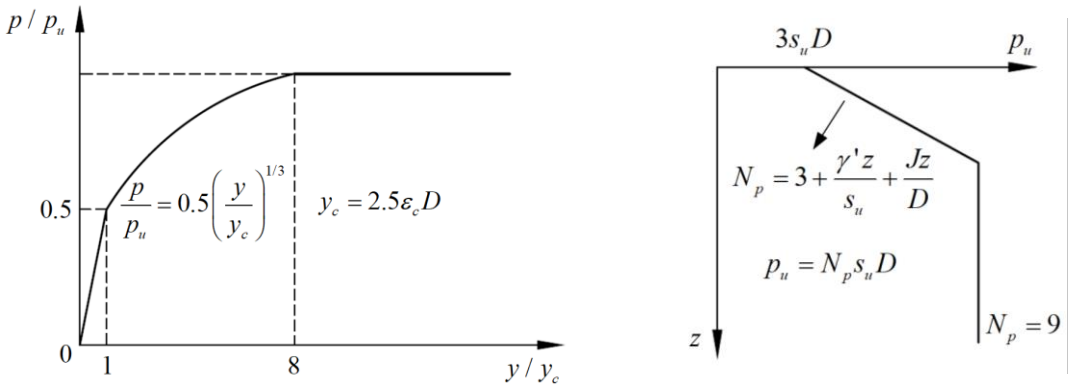


(a) Profile of normalized *p-y* curves (b) Ultimate lateral bearing capacity factor

**Fig.9** Traditional *p-y* curves method

To illustrate the limitations of the traditional *p-y* analysis methods in the API, this paper adopts the Winkle foundation model and the finite element analysis method to calculate the horizontal soil confinement of the pile at the mud line, the nonlinear soil stiffness is defined by the formulas presented in Fig.9. Fig.10 displays the comparative outcomes of various approaches. Furthermore, the ultimate bearing capacity captured by the traditional *p-y* analysis methods and the actual value obtained by the finite element analysis yields a ratio, which is defined to apparently reflect the deviation between the traditional *p-y* curves and the numerical method. Fig.11 depicts the ratio of the ultimate bearing capacity for thirteen different length-to-diameter ratios.

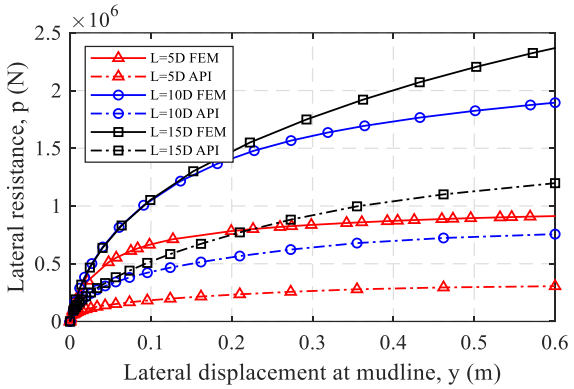


**Fig.10** Comparison between the traditional p-y method and finite element method

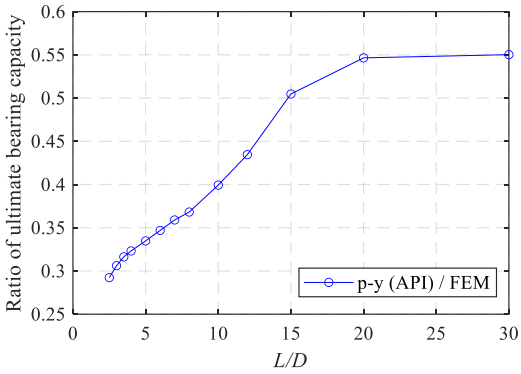


**Fig.11** Ultimate bearing capacity ratio

The comparison results in Fig.10 and Fig.11 show that the horizontal soil resistances calculated by traditional *p-y* curves are seriously underestimated for piles with different rigidities. The maximum deviation of the strongly rigid pile with $L/D$=2.5 exceeds 70% and more than 50% for other piles, and the deviation becomes significant with the increase of pile rigidity. The main cause is that the traditional *p-y* curves only involve the correlation between the lateral soil resistance and horizontal displacement without any rotational response. But failure mechanisms in Fig.8 reveal that for semi-rigid and rigid piles, the rotation of the soil near the pile bottom is the primary contributor to the lateral soil resistance. To precisely simulate the rigid pile-clay interaction, the soil rotational confinements have to be considered. It is also obvious from Fig.11 that the greater the length-to-diameter ratio, the higher the ratio of the ultimate bearing capacity, with an exponential correlation between them. The ultimate bearing capacity ratio no longer varies until $L/D$>20 (flexible pile). It is due to the part of the pile longer than the critical length will not affect the bearing capacity. Nevertheless, the ultimate bearing capacity of flexible piles calculated by traditional *p-y* curves still underestimates the soil constraint by 45%. From the formula of the p-y curves, it is known that the magnitude of ultimate capacity depends on the bearing capacity factor $N_p$. It is the underestimation of the bearing capacity factor of the normally consolidated clay that leads to the low calculation result.

In summary, traditional *p-y* curves have three limitations: (a) For the semi-rigid and rigid monopile, it only accounts for the horizontal restraint of soil without any rotational response, resulting in the lower ultimate bearing capacity of the monopile; (b) For the flexible pile, the ultimate bearing capacity factor is underrated, probably neglecting the suction of the clay; (c) The effects of strain hardening characteristics of the normally consolidated clay on the lateral resistance-displacement response are not taken into account. Thus, to accurately simulate the interaction between the normally consolidated clay and monopiles with different length-to-diameter ratios, traditional *p-y* curves must be modified.

## 4. Modified p-y curves for normally consolidated clay

### 4.1 Profile of modified p-y curves

To extract the lateral resistance at each depth section from the finite element model, the pile-soil normal and tangential contact stresses in the horizontal direction are integrated and summed along the pile perimeter according to Eq.(3):

$$p = \int_0^D \sigma_x dx + \int_0^D \tau_x dx \tag{3}$$

where $p$ is the lateral soil resistance per unit pile length at depth $z$; $\sigma_x$ is the normal stress on the pile node in the horizontal direction; $\tau_x$ is the tangential stress on the pile node in the horizontal direction; $x$ is the horizontal distance of the node from the center point of the pile. The normal and tangential contact forces can be output by the CNORMF and CSHEAR components in the horizontal direction in the ABAQUS.

To obtain the lateral soil resistance from elastic to plastic stages, this paper first analyzes the lateral resistance-displacement responses of monopiles with varying $L/D$ in the same penetration depth of $z$=0.5$D$, as shown in Fig.12. The depth is chosen precisely because the ultimate bearing capacity of piles with shallow penetration is lower, all the pile foundations including the case of $L/D$=2.5 can meet the fully plastic state condition. The outcomes shown in Fig.12 reveal that the *p-y* curves of piles with varying length-to-diameter ratios at the same penetration depth are almost identical. So the normalized lateral resistance-displacement curves only needs to be performed in a pile with a particular aspect ratio.

To capture the lateral resistance curves of piles with different penetration depths, a flexible pile with $L/D$=20 is selected with a horizontal displacement of 1.5m performed at the mud line to ensure that the upper soil reaches the fully plastic state. The result of the lateral soil resistance-displacement curves with $L/D$=20 at eight different penetration depths are shown in Fig.13. All the curves cover the horizontal section, which proves the soil in these eight depths has reached the plastic stage, and there is a direct correlation between penetration depth and soil resistance, with deeper depths resulting in greater resistance, but increase amplitudes are decreases.

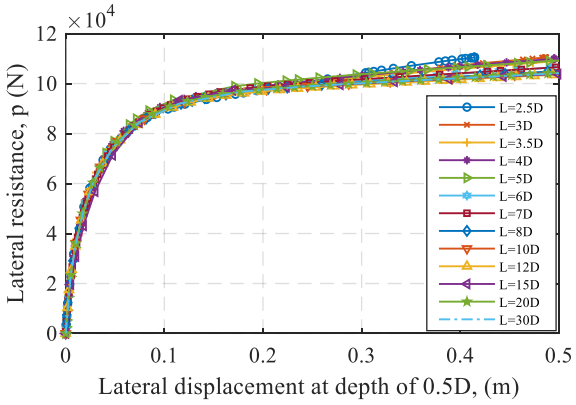


**Fig.12** P-y curves of piles with varying length-to-diameter ratio ($z$=0.5$D$)

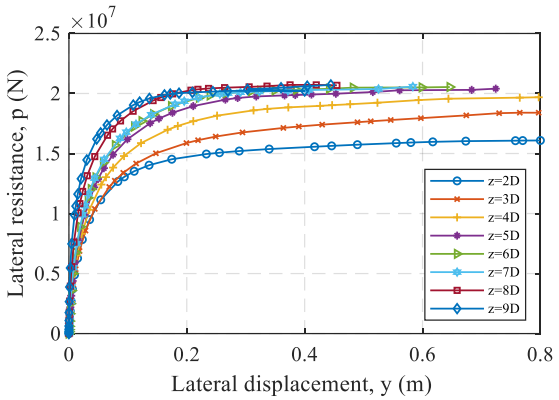


**Fig.13** P-y curves of piles with different penetration depths ($L/D$=20)

By normalizing the lateral soil resistance-displacement curves retrieved from the finite element model at different depths and comparing these curves with the representative *p-y* curve expressions shown in Table 3, formulas of *p-y* curve profiles for normally consolidated clay have been obtained, as shown in Fig.14, in which the dotted lines with hollow markers are the normalized curves extracted from the finite element model with $L/D$=20, and the dashed strings with solid marks are the proposed formulas. Obviously, the normalized *p-y* curves at various depths almost overlap and coincide with expressions of Zhang and Anderson [36] for both plastic stages and the initial stiffness in elastic stages and thus can be adopted as the recommended formulas for simulating the profile of *p-y* curves of soft clay.

**Table 3** Summary of representative *p-y* curves expressions

| References | Expressions of *p-y* curves |
|---|---|
| API (2014) | $p/p_u = 0.5(y/y_c)^{1/3} \quad y_c = 2.5\varepsilon_c D$ |
| Jeanjean (2009) | $\frac{p}{p_u} = \tanh\left(\frac{G_{max}}{100 s_u}\frac{y}{D}\right)^{0.5}$ |
| Zhang and Anderson (2017) | $\frac{p}{p_u} = \frac{\tau}{s_u} = \frac{2\sqrt{\gamma^p/\gamma_f^p}}{1+\gamma^p/\gamma_f^p} \quad \frac{y}{D} = 2.8\gamma^e + (1.35+0.25\alpha)\gamma^p$ |
| Wang et al. (2020) | $\frac{p}{p_u} = \tanh\left[\left(0.25D^2+0.23D+7.15\right)\left(\frac{y}{D}\right)^{0.017D+0.53}\right]$ |

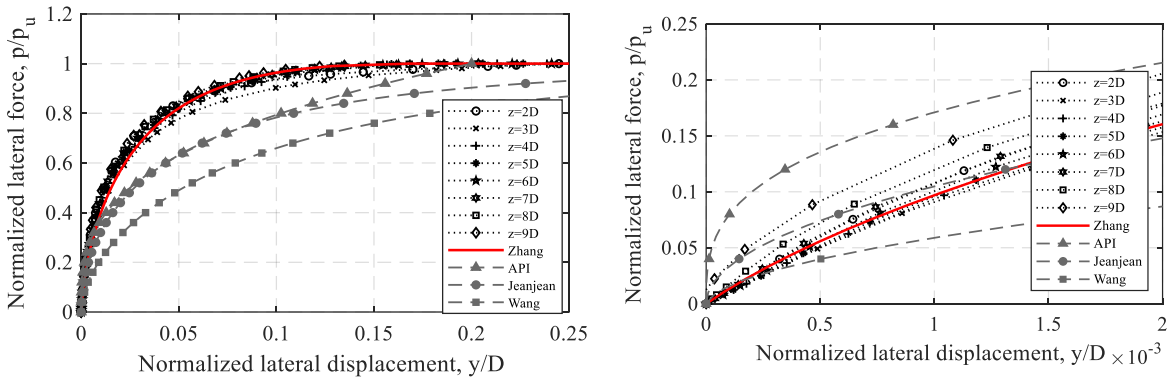


(a) The complete deformation process (b) Elastic deformation stage

**Fig.14** Comparison of dimensionless p-y curves

To verify the recommended *p-y* curves in soils with different strain hardening characteristics, horizontal motion behaviors of the semi-rigid pile with varying ultimate plastic shear strains were retrieved based on the Winkle foundation model. The finite element analyses in the same working conditions are also performed with $L/D$=6 at depth $z$=0.5$D$, as presented in Fig.15. The solid marks in the diagram are the finite element results and the strings of the three line types are the outcomes of the *p-y* curves method. Excellent agreements are obtained between the finite element analyses and the recommended analytical solution. It also appears that the elastic phase stiffness is controlled by $G_{max}/s_u$, and the strain hardening process is governed by $\gamma^p_f$. Consequently, the recommended lateral resistance-displacement relationship of the pile can be accurately calculated in geological conditions with any strain hardening level.

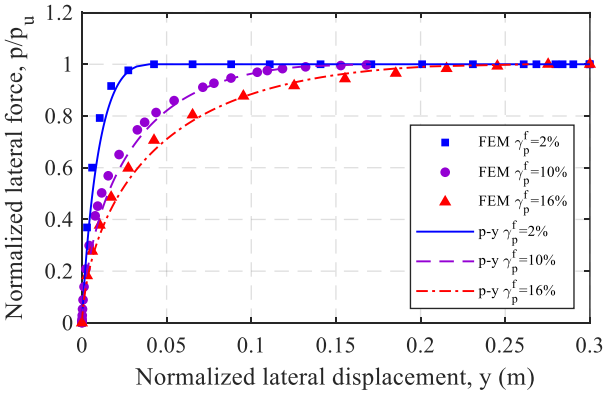


**Fig.15** Verification of recommended *p-y* curves with different ultimate plastic shear strains

The above conclusions also explain the unsuitability of other curves, The *p-y* curves advocated by API fail to capture the stress-strain relationship of the soil by parameter $\varepsilon_c$ alone, which leads to a curve with a large initial stiffness in the elastic phase, but too rapid rates of stiffness decrease, making the resistance low throughout the elastoplastic phase and causing a significant error. The expression proposed by Jeanjean [10] only has the elastic term $G_{max}/s_u$ without the plastic, which has a more suitable initial stiffness in the elastic phase but cannot describe the *p-y* relationship well in the elastoplastic phase. Wang et al's equations [29] exclusively examine the impact of monopile diameters without considering the stress-strain characteristics of the soil, which also results in obvious limitations.

## 4.2 Ultimate bearing capacity factor

The monopile ultimate bearing capacity factors $N_p$ extracted from the finite element analysis in different length-to-diameter ratios are compared with the representative calculation formulas summarized in Table.4 to get the most suitable expression of the normalized factor. The comparative results in Fig.16 illustrate that the ultimate bearing capacity factor profiles are almost consistent with a value of 2.6 near the soil surface and then increase with the penetration depth. Slopes of the ultimate bearing capacity factors decrease with the depth until greater than 5*D*, and the factor slowly converges to 10.5. Overall, the expression of Truong and Lehane matches well with the numerical simulation results.

**Table 4** Summary of representative expressions of the ultimate bearing capacity factor

| References | Expressions of the bearing capacity factor | $N_{pd}$ |
|---|---|---|
| API (2014) | $N_p = 3 + \frac{Jz}{D} + \frac{\gamma' z}{s_u} \le 9$ | 9 |
| Jeanjean (2009) | $N_p = 12 - 4e^{(-\xi z/D)} \quad \xi = 0.25 + 0.05 \cdot \frac{s_{u0}}{kD}$ | 12 |
| Zhang et al. (2016) | $N_p = 2\left\{11.94 - 8.72\left[1 - \left(\frac{z/D}{14.5}\right)^{0.6}\right]^{1.35}\right\}$ | 11.94 |
| Truong and Lehane (2018) | $N_p = 10.5\left[1 - 0.75e^{\left(\frac{-0.6z}{D}\right)}\right]$ | 10.5 |

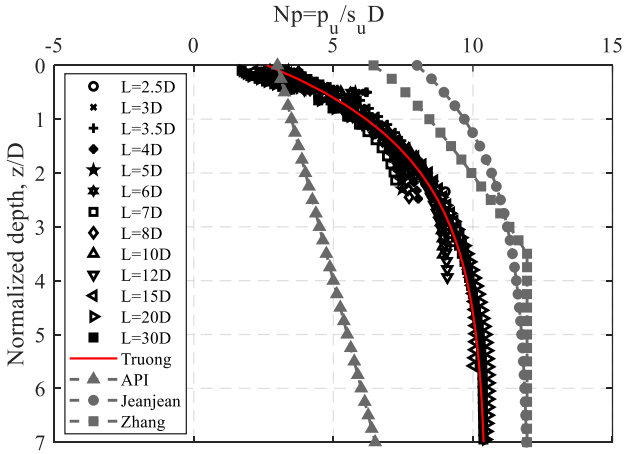


**Fig.16** Comparison of bearing capacity factors

The bearing capacity factors reach the ultimate value $N_{pd}$ when the penetration depths increase to the point that the full flow mechanism occurs in the surrounding soil. $N_{pd}$ values

for each calculated expression are summarized in Table.4. Among them, the largest value of the bearing capacity factor in API is 9, which is much smaller than the values obtained in other studies, and this is the root of underestimations of the bearing capacities. It is worth mentioning that test conditions in the API are over-consolidated clay where the pile-soil separation is allowed, while this paper investigates the normally consolidated soft clay that needs to consider the soil suction. In the present paper, the lateral responses of the pile in both overconsolidated and normally consolidated clay are simulated, and displacement and stress nephograms around the piles are shown in Fig.17 and Fig.18, respectively. For the over-consolidated clay shown in Fig.17, the pile is separated from the back soil and generates a gap under the horizontal displacement, and the wedge-type flow is only present on one side of the pile. However, for the case of normally consolidated clay shown in Fig.18, the active and passive wedge-type mechanisms of the soil present simultaneously because of the consideration of the suction condition, and the ultimate bearing capacity factor in this circumstance is twice as large as that for one side wedge-type flow, which is in accordance with the conclusion of Zhang et al [23]. And it further proves the unsuitability of the API recommended method for normally consolidated clay soils.

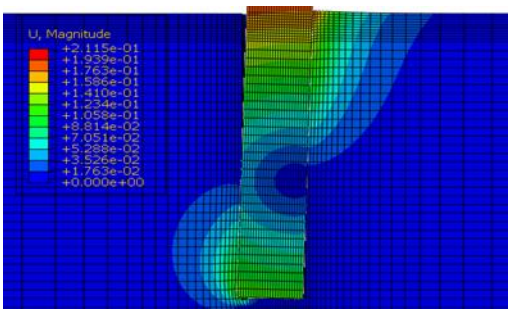


**Fig.17** Displacement nephogram without suction

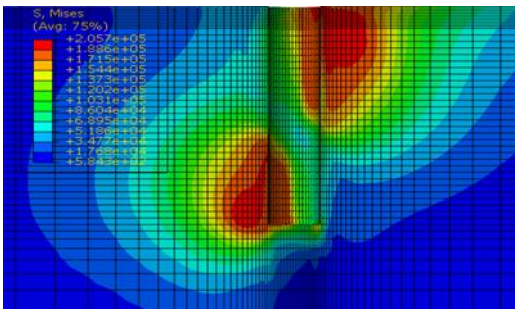


**Fig.18** Stress nephogram in suction conditioon

## 4.3 Bearing capacity of monopiles calculated by modified p-y curves

By comparing the data trend lines of finite element analysis with the representative expressions, the modified *p-y* curves are determined, for which the normalized *p-y* profile adopts the formula suggested by Zhang et al [26], and the ultimate bearing capacity factor is the recommended value by Truong et al [12]. The schematic diagrams and expressions of modified p-y curves are displayed in Table 5. Fig.19 presents the lateral soil resistances extracted from the Winkle foundation model, in which the nonlinear soil stiffness at different penetration depths are obtained by discrete these expressions. The corresponding finite element results are also plotted in the diagrams.

To visually reflect the correction effect of the modified *p-y* curves, the ultimate bearing capacity ratios are specified by yielding the ultimate bearing capacity of the revised *p-y* curves and the actual value of finite element analysis, as shown in Fig.20. Overall, modified *p-y* curves can improve the soil confinement significantly. The predictive accuracy of the ultimate bearing capacity for this method has been proved by which the errors of the ultimate bearing capacity are less than 2% for flexible piles with *L/D*=30, 20, and 15, and the maximum error counted in the elastic deformation phase does not exceed 3%. Since the impact of soil strain hardening characteristics on the pile lateral response is fully considered in this paper, the modified *p-y* curves can apply to soils with different hardening properties.

**Table 5** Summary of the modified *p-y* curves

| Description |
|---|
| 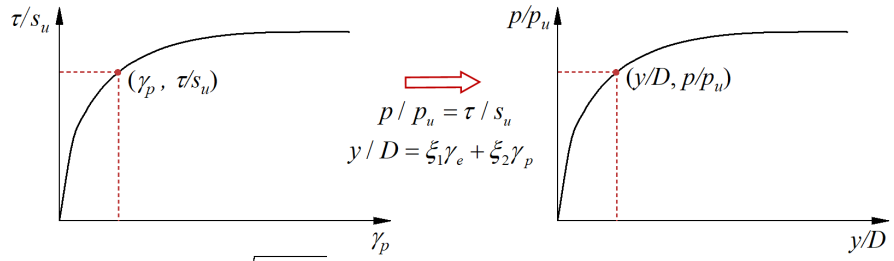 <br>$p/p_u = \tau/s_u$<br>$y/D = \xi_1\gamma_e + \xi_2\gamma_p$<br>$\frac{p}{p_u} = \frac{\tau}{s_u} = \frac{2\sqrt{\gamma_p/\gamma_f^p}}{1+\gamma_p/\gamma_f^p}$ $\quad p_u = N_p s_u D = 10.5\left[1-0.75e^{-0.6z/D}\right]s_u D$<br>$\frac{y}{D} = \xi_1\gamma_e + \xi_2\gamma_p \quad \xi_1 = 2.6 \quad \xi_2 = 1.35+0.25\alpha \quad \gamma_e = \frac{\tau/s_u}{G_{\max}/s_u}$ |

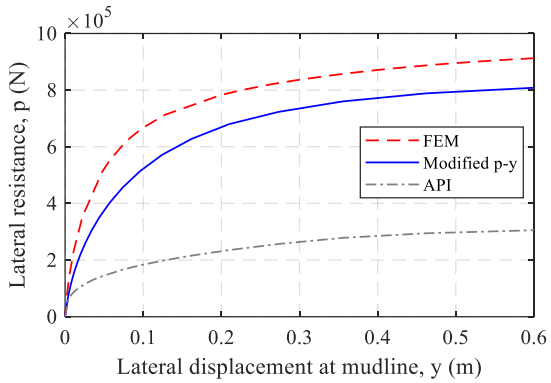


(a) *L*/*D*=5

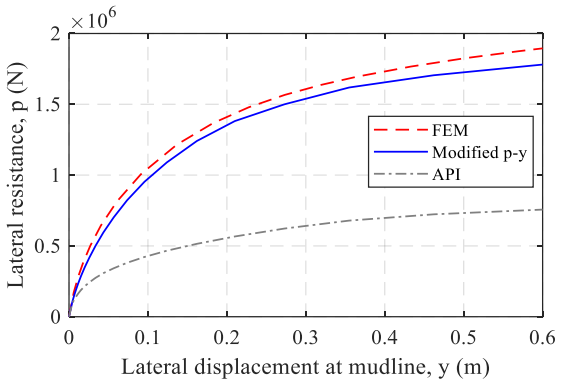


(b) *L*/*D*=10

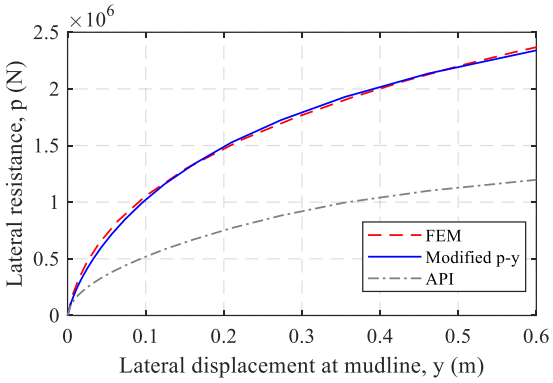


(c) *L*/*D*=15

**Fig.19** Verification of lateral soil resistance

However, there are still underestimations of about 15% for the ultimate bearing capacity of the rigid monopiles, which is due to the fact that the rigid monopile is dominated by the rotational motion, and the additional soil confinement on the pile should be accounted [11, 28, 34, 41]. The emphasis of this paper is on the simulation of the lateral soil resistance and modification of the p-y curves in API. For rigid piles, the adoption of the modified *p-y* curves improves the bearing capacity by more than 150% and reduces the error by about 80% compared with the traditional *p-y* curve method, so the modified expressions can be used in combination with other confinement curves or as an approximate estimation method.

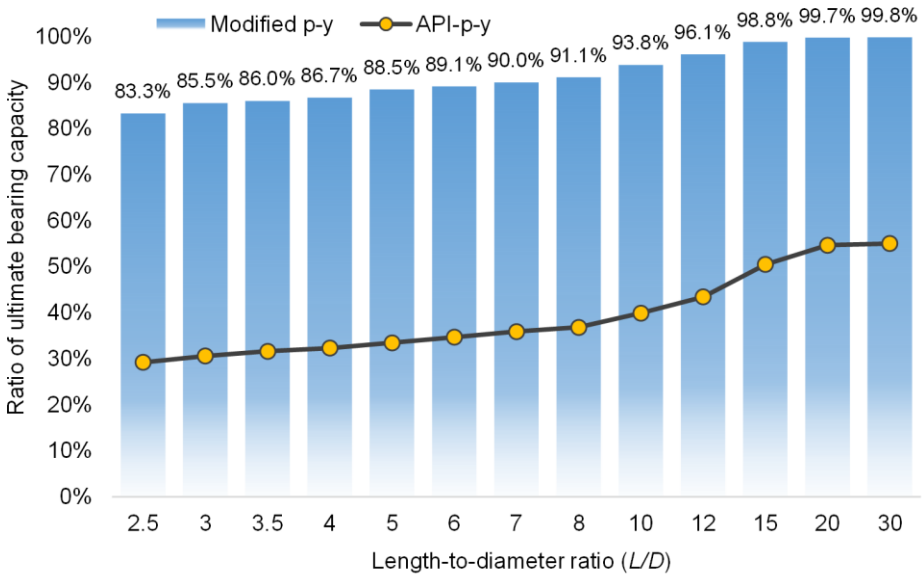


**Fig.20** Deviation of the ultimate bearing capacity ratio

## 5. Conclusions

In the present paper, a 3D pile-soil interaction finite element model was performed considering the soil suction and strain hardening characteristics. Adjustments were made to the *p-y* analysis method advocated by API after conducting the finite element analysis with different length-to-diameter ratios. The accurate and efficient modified *p-y* curves were proposed for simulating the interaction between the normally consolidated clay and monopiles and assessing the ultimate bearing capacity of piles. The specific conclusions are as follows:

(1) The *p-y* curves in API significantly underestimate the confinement of the soil. For the ultimate bearing capacity of a semi-rigid pile, using this method will underestimate the error by more than 50%; for strongly rigid piles, the error caused is more than 70%; and for flexible piles, using the traditional p-y curves will produce an error of 45%.

(2) The failure mechanisms of the surrounding soil of piles with different length-to-diameter ratios are clarified. Comprehensive consideration of soil failure mechanisms and the effects of stress-strain characteristics on the bearing capacity of monopiles, three limitations of the *p-y* curves in API are summarized, which are underestimating the lateral soil confinement, failing to account for the soil confinement in other directions, and neglecting the effects of the soil stress-strain relationship.

(3) Modified *p-y* curves are qualified for sufficiently considering the lateral soil confinement, and the error is less than 3% for flexible piles so that it can be employed as the design basis for lateral resistance-displacement response and ultimate bearing capacity of flexible piles. For rigid piles and semi-rigid piles, this method can be used as an expression for horizontal resistance in combination with other confinement curves.

## ACKNOWLEDGEMENT

This work was supported by the National Natural Science Foundation of China [Grant Nos. 51890915, 52071301 and 52101333]; the Fundamental Research Funds for the Central Universities.

## REFERENCES

[1] GWEC, 2022. Global wind report. https://gwec.net/global-wind-report-2022

[2] Cheng, Y., Fu, L., Dai, S. S., Collu, M., Ji, C. Y., Yuan, Z.M., 2022. Experimental and numerical investigation of WEC-type floating breakwaters: A single-pontoon oscillating buoy and a dual-ponton oscillation water column. *Coastal Engineering*, 177, 104188. https://doi.org/10.1016/j.coastaleng.2022.104188

[3] Cheng, Y., Fu, L., Dai, S. S., Collu, M., Cui, L., Yuan, Z. M., 2022. Experimental and numerical analysis of hybrid WEC-breakwater system combining an oscillating water column and an oscillating buoy. *Renewable and Sustainable Energy Reviews*, 160, 112909. https://doi.org/10.1016/j.rser.2022.112909

[4] Soares, C., Bhattacharjee, J., Karmaker, D., 2014. Overview and prospects for development of wave and offshore wind energy. *Brodogradnja*, 65(2), 87-109.

[5] Veic, D., Sulisz, W., Soman, R., 2019. Effect of breaking wave shape on impact load on a monopile structure. *Brodogradnja*, 70(2), 25-42. https://doi.org/10.21278/brod70302

[6] Liu, L. Q., Jin, W. C., Gao, Y., 2017. Dynamic analysis of a truss spar-type floating foundation for 5MW vertical-axis wind turbine. *Journal of Offshore Mechanics and Arctic Engineering*, 139, 061902. https://doi.org/10.1115/1.4037292

[7] Deng, W. R., Gao, X. F., Liu, L. Q., Zhao, H. X., 2018. Dynamic modeling of H-type floating VAWT considering the Rigid-Flexible Coupling motions. *Proceedings of the ASME 2018 37th International Conference on Ocean, Offshore and Arctic Engineering*, Madrid, Spain, OMAE2018-78619. https://doi.org/10.1115/OMAE2018-78619

[8] Guo, Q., Ma, G., Sun, L. P., Wang, H. W., 2015. Dynamic response analysis of a triangular tension leg platform. *Proceedings of the ASME 2015 34th International Conference on Ocean, Offshore and Arctic Engineering*, Newfoundland, Canada, OMAE2015-41480. https://doi.org/10.1115/OMAE2015-41480

[9] Fowai, I., Zhang, J. H., Sun, K., Wang, B., 2021. Structural analysis of jacket foundations for offshore wind turbines in transitional water. *Brodogradnja*, 72(1), 109-124. https://doi.org/10.21278/brod72106

[10] Jeanjean, P., 2009. Re-assessment of p-y curves for soft clays from centrifuge testing and finite element modeling. *Proceedings of Offshore Technology Conference*, Houston, USA, OTC20158. https://doi.org/10.4043/20158-MS

[11] Qi, W. G., Gao, F. P., Randolph, M. F., Lehane, B. M., 2016. Scour effects on p–y curves for shallowly embedded piles in sand. *Géotechnique*, 66(8), 648-660. https://doi.org/10.1680/jgeot.15.P.157

[12] Hong, Y., He, B., Wang, L. Z., Wang, Z., Ng, C. W. W., Masin, D., 2017. Cyclic lateral response and failure mechanisms of semi-rigid pile in soft clay: centrifuge tests and numerical modelling. *Canadian Geotechnical Journal*, 54(6), 806-824. https://doi.org/10.1139/cgj-2016-0356

[13] Truong, P., Lehane, B. M., 2018. Effects of pile shape and pile end condition on the lateral response of displacement piles in soft clay. *Géotechnique*, 68(9), 798-804. https://doi.org/10.1680/jgeot.16.P.291

[14] Byrne, B. W., McAdam, R., Burd, H. J., Houlsby, G. T., Martin, C. M., 2015. New design methods for large diameter piles under lateral loading for offshore wind applications. *International Symposium on Frontiers in Offshore Geotechnics*, London. https://doi.org/10.1201/b18442-96

[15] Zhu, B., Zhu, Z. J., Li, T., Liu, J. C., Liu, Y. F., 2017. Field tests of offshore driven piles subjected to lateral monotonic and cyclic loads in soft clay. *Journal of Waterway, Port, Coastal and Ocean Engineering*, 143(5): 5017003. https://doi.org/10.1061/(ASCE)WW.1943-5460.0000399

[16] Randolph, M. F., Houlsby, G. T., 1984. The limiting pressure on a circular pile loaded laterally in cohesive soil. *Géotechnique*, 34(4), 613-623. https://doi.org/10.1680/geot.1984.34.4.613

[17] Murff, J. D., Hamilton, J. M., 1993. P-ultimate for undrained analysis of laterally loaded piles. *Journal of Geotechnical Engineering*, 119(1), 91-107. https://doi.org/10.1061/(ASCE)0733-9410(1993)119:1(91)

[18] Martin, C. M., Randolph, M. F., 2006. Upper bound analysis of lateral pile capacity in cohesive soil. *Géotechnique*, 56(2), 141-145. https://doi.org/10.1680/geot.2006.56.2.141

[19] Yu, J., Huang, M. S., Zhang, C. R., 2015. Three-dimensional upper-bound analysis for ultimate bearing capacity of laterally loaded rigid pile in undrained clay. *Canadian Geotechnical Journal*, 52(11), 1775-1790. https://doi.org/10.1139/cgj-2014-0390

[20] Meng, K., Cui, C. Y., Liang, Z. M., Li, H. J., Pei, H. F., 2022. A new approach for longitudinal vibration of a large-diameter floating pipe pile in visco-elastic soil considering the three-dimensional wave effects. *Computers and Geotechnics*, 128, 103840. https://doi.org/10.1016/j.compgeo.2020.103840

[21] Cui, C. Y., Liang, Z. M., Xu, C. S., Xin, Y., Wang, B. L., 2023. Analytical solution for horizontal vibration of end-bearing single pile in radially heterogeneous saturated soil. *Applied Mathematical Modelling*, 116, 65-83. https://doi.org/10.1016/j.apm.2022.11.027

[22] DNV, 2016. DNVGL-ST-0126: Support structure for wind turbines.

[23] Templeton, J. S., 2009. Finite element analysis of conductor/seafloor interaction.. *Proceedings of Offshore Technology Conference*, Houston, USA, OTC20197. https://doi.org/10.4043/20197-MS

[24] Zhang, Y. H., Andersen, K. H., Tedesco, G., 2016. Ultimate bearing capacity of laterally loaded piles in clay-some practical considerations. *Marine Structures*, 50, 260-275. https://doi.org/10.1016/j.marstruc.2016.09.002

[25] Terceros, M., Achmus, M. A., Thieken, K., 2017. Evaluation of p-y approaches for piles in soft clay. *Proceedings of Offshore Site Investigation Geotechnics 8th International Conference Proceeding*, Guildford, 724-731. https://doi.org/10.3723/OSIG17.724

[26] Murphy, G., Igoe, D., Doherty, P., Gavin, K., 2018. 3D FEM approach for laterally loaded monopile design. *Computers and Geotechnics*, 100, 76-83. https://doi.org/10.1016/j.compgeo.2018.03.013

[27] He, B., Lai, Y. Q., Wang, L. Z., Hong, Y., Zhu, R. H., 2019. Scour effects on the lateral behavior of a large-diameter monopile in soft clay: role of stress history. *Journal of Marine Science and Engineering*, 7,170. https://doi.org/10.3390/jmse7060170

[28] Zhang, C., Kang, Z., Ma, Gang, Xu, X., 2019. Mechanical modeling of deepwater flexible structures with large deformation based on absolute nodal coordinate formulation. *Journal of Marine Science and Technology*, 24, 1241-1255. https://doi.org/10.1007/s00773-018-00621-0

[29] Wang, L. Z., Lai, Y. Q., Hong, Y., Masin, D., 2020. A unified lateral soil reaction model for monopiles in soft clay considering various length-to-diameter (*L/D*) ratios. *Ocean Engineering*, 2020, 212, 107492. https://doi.org/10.1016/j.oceaneng.2020.107492

[30] Zhou, X. K., Chen, J. H., Ge, Z. G., Zhao, T., Li, W. H., 2022. Numerical investigations on the effects of seabed shallow soils on a typical deepwater subsea wellhead system. *Brodogradnja*, 73(3), 1-19. https://doi.org/10.21278/brod73301

[31] Cui, C. Y., Meng, K., Xu, C. S., Wang, B. L., Xin, Y., 2022. Vertical vibration of a floating pile considering the incomplete bonding effect of the pile-soil interace. *Computers and Geotechnics*, 150, 104894. https://doi.org/10.1016/j.compgeo.2022.104894

[32] API, 2014. Recommended Practice 2GEO. Geotechnical and Foundation Design Considerations.

[33] Matlock, H.,1970. Correlation for design of laterally loaded piles in soft clay. *Proceedings of Offshore Technology Conference*, Austin. https://doi.org/10.4043/1204-MS

[34] Fu, D. F., Zhang, Y. H., Aamodt, K. K., Yan, Y., 2020. A multi-spring model for monopile analysis in soft clays. *Marine Structures*, 72, 102768. https://doi.org/10.1016/j.marstruc.2020.102768

[35] O'Neill, M. W., Gazioglu, S. M., 1984. Evaluation of p-y relationships in cohesive soil. *Proceedings of analysis and design of pile foundations*, ASCE, Houston, Texas. https://doi.org/10.4043/1204-MS

[36] Zhang, Y. H., Andersen, K. H., 2017. Scaling of lateral pile p-y response in clay from laboratory stress-strain curves. *Marine Structures*, 53, 124-135. https://doi.org/10.1016/j.marstruc.2017.02.002

[37] Zhang, Y. H., Andersen, K H., 2019. Soil reaction curves for monopiles in clay. *Marine Structures*, 65, 94-113. https://doi.org/10.1016/j.marstruc.2018.12.009

[38] Grimstad, G., Andresen, L. P., Jostad, H., 2012. NGI-ADP: Anisotropic shear strength model for clay. *International Journal for Numerical and Analytical Methods in Geomechanics*, 36(4):483-497. https://doi.org/10.1002/nag.1016

[39] Dassault Systemes, 2014. ABAQUS, version 6.14.

[40] Poulos, H. G., Hull, T. S., 1989. The role of analytical geomechanics in foundation engineering. *Proceedings of Foundation Engineering: Current Principles and Practices*, New York.

[41] Lai, Y. Q., Wang, L. Z., Zhang, Y. H., Hong, Y., 2021. Site-specific soil reaction model for monopiles in soft clay based on laboratory element stress-strain curves. *Ocean Engineering*, 220, 108437. https://doi.org/10.1016/j.oceaneng.2020.108437

Submitted: 20.03.2023.
Accepted: 27.04.2023.

[a,b] Bin Wang, binwangdut@outlook.com
[c] Yuqi Jiao, jiaoyq@mail.dlut.edu.cn
[c] Dongsheng Qiao*, corresponding author, qiaods@dlut.edu.cn
[a,b] Shan Gao, gao_s3@hdec.com
[d,b] Tianfei Li, li_tf@hdec.com
[c] Jinping Ou, oujinping@dlut.edu.cn
[a] Key Laboratory of Far-shore Wind Power Technology of Zhejiang Province, Hangzhou 311122, China
[b] Powerchina Huadong Engineering Corporation Limited, Hangzhou 311122, China
[c] State Key Laboratory of Coastal and Offshore Engineering, Dalian University of Technology, Dalian 116024, China
[d] Huadong Eco-Environmental Engineering Research Institute of Zhejiang Province, Hangzhou 311122, China